

Higher-Order Topological Insulators via Momentum-Space Nonsymmorphic Symmetries

Jinbing Hu^{1,2}, Songlin Zhuang,² and Yi Yang^{1,*}

¹*Department of Physics and HK Institute of Quantum Science and Technology,
The University of Hong Kong, Pokfulam, Hong Kong, China*

²*College of Optical-Electrical Information and Computer Engineering,
University of Shanghai for Science and Technology, Shanghai 200093, China*

 (Received 6 July 2023; accepted 19 April 2024; published 22 May 2024)

We theoretically construct a higher-order topological insulator (HOTI) on a Brillouin real projective plane enabled by momentum-space nonsymmorphic (\mathbf{k} – NS) symmetries from synthetic gauge fields. Two anticommutative \mathbf{k} – NS glide reflections appear in a checkerboard \mathbf{Z}_2 flux model, impose nonsymmorphic constraints on Berry curvature, and quantize bulk and Wannier-sector polarization nonlocally across different momenta. The model's bulk exhibits an isotropic quadrupole phase diagram, where the transition appears intrinsically from bulk gap closure. The model hosts the simultaneous presence of intrinsic and extrinsic HOTI features: in a ribbon geometry where one pair of boundaries gets open, the edge termination can induce boundary-obstructed topological phase within the symmetry-protected topological phase due to the breaking of \mathbf{k} – NS symmetry. At last, we present a concrete design for the real projective plane quadrupole insulator and show how to measure the momentum glide reflection based on acoustic resonator arrays. Our results shed light on HOTIs on deformed Brillouin manifolds via \mathbf{k} – NS symmetries.

DOI: [10.1103/PhysRevLett.132.213801](https://doi.org/10.1103/PhysRevLett.132.213801)

Crystalline symmetries play a crucial role in stabilizing topological insulators and semimetals in solids and artificial materials. Combined with the three internal symmetries, topological classification can be further refined via symmorphic (like inversion, reflection, and proper rotations) [1–4] and nonsymmorphic symmetries [5–10] beyond the tenfold way [11,12]. While nonsymmorphic symmetries traditionally refer to screw rotations and glide reflections accompanied by fractional lattice translation in real space, recently their counterparts have been identified in momentum space [13], known as the momentum-space nonsymmorphic (\mathbf{k} – NS) symmetries. The key to creating \mathbf{k} – NS symmetries is synthetic gauge fields [14], which can projectively modify point-group symmetries into space-group ones [13,15,16]. Since operating in momentum space, \mathbf{k} – NS symmetries can modify the topology of the Brillouin zone (BZ). For example, the BZ torus was transformed into a Brillouin Klein bottle under a single \mathbf{k} – NS symmetry [13], leading to nonlocal first-order topology. It is thus pertinent to seek the construction of higher-order topology via \mathbf{k} – NS symmetries on versatile BZ manifolds.

The electric polarization of crystals [17–19] was recently extended to higher electric multipole moments, giving rise to higher-order topological insulators (HOTIs) [20–22], which has been observed in various physical platforms (e.g., Refs. [23–29]). Moreover, the appearance of corner charges has been distilled via the distinction of intrinsic and extrinsic HOTIs [30–32] that are associated with

symmetry-protected topological phase (SPTP) and boundary-obstructed topological phase (BOTP), respectively. In particular, the quadrupole phase was realized in real-space nonsymmorphic systems, where quantized quadrupole moment is protected by glide reflections [33–37]. However, higher-order band topology has not been realized by \mathbf{k} – NS symmetries, and the associated unique features have not been discussed.

In this Letter, we theoretically introduce a quadrupole topological insulator via two anticommutative \mathbf{k} – NS symmetries on a two-dimensional Brillouin real projective plane ($\mathbb{R}P^2$). The two \mathbf{k} – NS reflections, which emerge from \mathbf{Z}_2 gauge fields and the associated checkerboard flux pattern, partition the original BZ torus into several non-unique $\mathbb{R}P^2$ manifolds. They impose nonsymmorphic constraints on the energy bands and Berry curvature and quantize bulk and Wannier-sector polarizations nonlocally in momentum space. The system exhibits coexistence of intrinsic and extrinsic HOTI features. In the bulk, the quadrupole moment is induced by bulk gap closures and protected by the \mathbf{k} – NS symmetries. In cylinders, edge polarization can be created via two means: first, SPTP transition of *bulk* gap closures can occur due to hopping variation along the *open* direction; second, BOTP transition of *edge* gap closures can occur due to hopping strength variations along the *periodic* direction. In our proposal, we show that the half-translation of the \mathbf{k} – NS symmetry can be measured via momentum-resolved edge modes localized on the opposite ends of a sample.

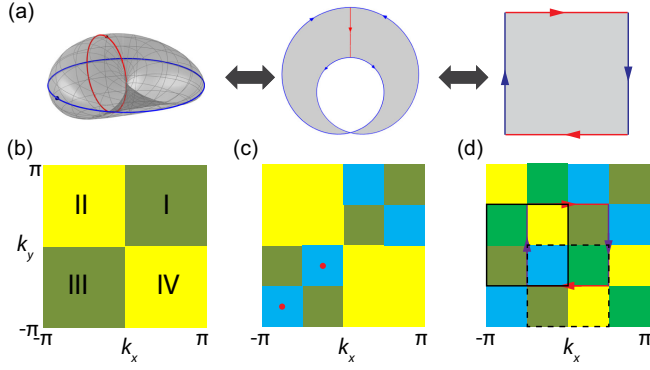


FIG. 1. Real projective plane in momentum space. (a) Folding a real projective plane (left) from a rectangle (right), whose opposite sides are glued in an antiparallel manner (denoted by color arrows). (b) The \mathbf{k} -NS mirror symmetries M_x and M_y divide the first Brillouin zone (BZ) $[-\pi, \pi] \times [-\pi, \pi]$ into four quadrants I-IV. (c) The \mathbf{k} -NS inversion P_π further divides each quadrant into diagonal and antidiagonal partners (e.g., green and blue colors in the I and III quadrants). The red dots indicate two momenta linked by P_π . (d) M_x , M_y , and P_π jointly divide the first BZ into 16 plaquettes. A reduced BZ can be defined using any four plaquettes of distinct colors, e.g., the square at the zone center surrounded by red and violet arrows. Other examples include the squares in black solid and dashed lines.

Brillouin real projective plane.— RP^2 is a two-dimensional surface generalizing the Möbius strip. It is constructed from a square by identifying two pairs of opposite edges with a half twist [Fig. 1(a)]. Mathematically, the construction of RP^2 can be represented as a unit square $([0, 1] \times [0, 1])$ with opposite edges following the equivalence relations

$$(x, 0) \sim (1 - x, 1) \quad \text{for } 0 \leq x \leq 1, \quad (1a)$$

$$(0, y) \sim (1, 1 - y) \quad \text{for } 0 \leq y \leq 1. \quad (1b)$$

We aim to realize these conditions to realize RP^2 in momentum space. The \mathbf{k} -NS reflections M_x and M_y meet the need, as they perform glide reflection in momentum space:

$$M_x: (k_x, k_y) \rightarrow (-k_x, k_y + \pi), \quad (2a)$$

$$M_y: (k_x, k_y) \rightarrow (k_x + \pi, -k_y), \quad (2b)$$

which realizes Eq. (1) for $\mathbf{k} \equiv (k_x, k_y) \in [-\pi/2, \pi/2] \times [-\pi/2, \pi/2]$ (see Sec. S1 of [38]). In addition, the simultaneous presence of M_x and M_y naturally defines a \mathbf{k} -NS inversion $P_\pi \equiv M_x M_y$, which confines the wave vectors as

$$P_\pi: (k_x, k_y) \rightarrow (\pi - k_x, \pi - k_y). \quad (3)$$

M_x , M_y , and P_π further partition the Brillouin torus. Specifically, M_x and M_y divides the first BZ

into four quadrants [Fig. 1(b)]. Further, each quadrant is divided into two pairs by P_π : the diagonal and off-diagonal pairs, and each pair is linked by P_π [Fig. 1(c)]. Therefore, M_x , M_y , and P_π jointly divide the first BZ into 16 plaquettes [Fig. 1(d)] (see Sec. S2 of [38]). A reduced BZ can be defined on any four plaquettes of distinct colors, e.g., the four plaquettes $(k_x, k_y) \in [-\pi/2, \pi/2] \times [-\pi/2, \pi/2]$ at the zone center in Fig. 1(d). Notably, the boundaries of the reduced BZ connect in an antiparallel manner via M_x (red arrows) and M_y (violet arrows), thereby realizing an RP^2 in momentum space. There are four remarkable features of the \mathbf{k} -NS symmetry group. First, analogous to their real-space counterparts, the \mathbf{k} -NS symmetries exhibit rich Abelian and non-Abelian algebra depending on the (anti)commutation between M_x and M_y [34,47–51]. Second, the choice of the reduced RP^2 BZ is nonunique [e.g., squares in black solid and dashed lines in Fig. 1(d), as long as four plaquettes in distinct colors are enclosed]. Third, the reduced RP^2 BZ remains a closed manifold, enabling adiabatic calculation of topological invariants. Fourth, at the reduced BZ corner, the \mathbf{k} -NS inversion exhibits four nonsymmorphic inversion invariant momenta $(\pm\pi/2, \pm\pi/2)$, and their symmetry eigenvalues can be used for topology analysis (see Sec. S3 of [38]). A topological invariant χ can be defined for nonsymmorphic inversion (similar to the Fu-Kane formula [52] for conventional inversion)

$$e^{i2\pi\chi} = \prod_{i=1}^4 \Gamma_i, \quad (4)$$

where Γ_i is the P_π eigenvalue(s) of the occupied bands at the i th nonsymmorphic inversion invariant momentum.

Tight-binding model.—Consider the square lattice of four sites [Fig. 2(a)], the presence of π flux enables an anticommutative relation between reflection M_x and the translation operator L_y along y , i.e., $M_x L_y M_x^{-1} L_y^{-1} = -1$. The right-hand negative sign can be reformulated as a half-translation along k_y , i.e., $-1 = e^{iG_y a/2}$ (where a is the lattice constant and G_y the reciprocal lattice vector along y) [13]. Therefore, besides reversing k_x , M_x also contains a half-translation along k_y , fulfilling Eq. (2a). Similarly, the relation Eq. (2b) can be implemented by adding π flux via a different gauge connection in Fig. 2(b). Jointly, we arrange the negative hopping along both x and y directions [Figs. 2(a) and 2(b)] to realize a checkerboard flux pattern [Fig. 2(c)] featuring \mathbf{k} -NS M_x and M_y . The associated Bloch Hamiltonian is

$$H(k_x, k_y) = \begin{bmatrix} 0 & a_+ & b_+ & 0 \\ a_+^* & 0 & 0 & b_- \\ b_+^* & 0 & 0 & a_- \\ 0 & b_-^* & a_-^* & 0 \end{bmatrix}, \quad (5)$$

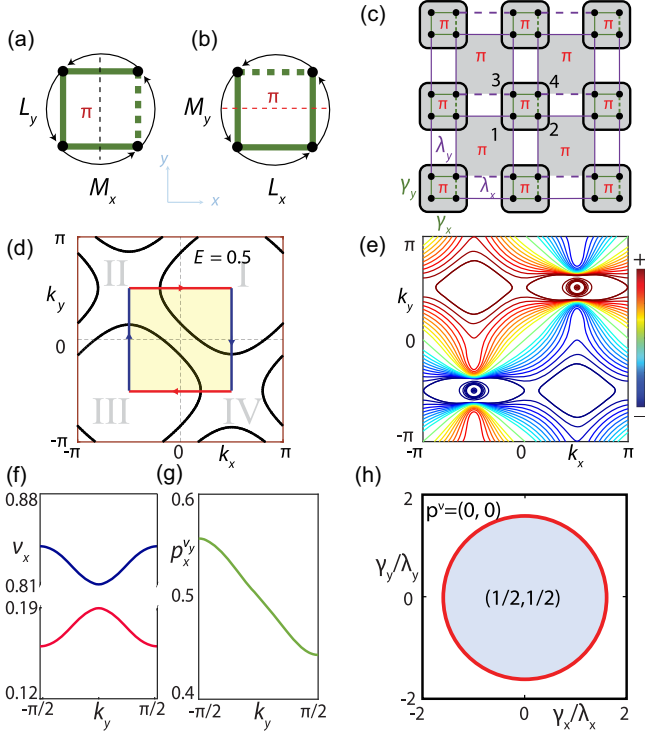


FIG. 2. Lattice model for nonsymmorphic reflections and inversion in momentum space. (a),(b) Threading π flux projectively modifies the conventional reflections m_i ($i = x, y$) into \mathbf{k} -NS ones M_i ($i = x, y$), which anticommute with the translational symmetries L_j ($j = y, x$) along the other direction. (c) Model with checkerboard π flux enables anticommutative M_x and M_y and their product P_π . Solid and dashed lines indicate real positive and negative hoppings. (d) The entire iso-energy contour (at $E = 0.5$) can be constructed by that within the reduced RP^2 BZ (shaded yellow). (e) Nonsymmorphic Berry curvature of the lowest band. (f),(g) Nonlocal constraints on the Wannier centers ν_x [(f); also see Eq. (8)] and Wannier-sector polarization p_x^y [(g); also see Eq. (9a)]. (h) Isotropic binary bulk phase diagram showing the quadrupole $\mathbf{p}^v = (1/2, 1/2)$ within phase boundary (red circle) associated with bulk gap closure. $\gamma_x = 0.75$ and $\gamma_y = 0.68$ are consistently used for (d)–(g).

with $a_\pm = \gamma_x \pm \lambda_x e^{-ik_x}$, $b_\pm = \pm\gamma_y + \lambda_y e^{-ik_y}$, and $*$ denoting complex conjugate. Here, γ_x and γ_y (λ_x and λ_y) represent the intracell (intercell) hopping amplitudes along x and y , respectively. Without loss of generality, we set unity lattice constants and $\lambda_x = \lambda_y = 1$. Under the link arrangements in Fig. 2(c), the \mathbf{k} -NS symmetries satisfying Eqs. (2) and (3) have the form: $M_x = \sigma_3 \otimes \tau_1$, $M_y = \sigma_1 \otimes \tau_0$, and $P_\pi = i\sigma_2 \otimes \tau_1$, together generating a non-Abelian group D_8 . Here, σ 's and τ 's are Pauli matrices acting on sites along y and x , respectively.

The consequence of the \mathbf{k} -NS symmetries can be seen from the energy bands and Berry curvatures. An example energy contour validates the BZ partition in Fig. 2(d), where the band in the reduced RP^2 BZ can be extended to generate that of the full BZ (see Sec. S4 of [38]). Such

shrinking of the BZ results from the gauge transformation induced by the negative coupling, which doubles the lattice constant along x and y (see Sec. S5 of [38]). The \mathbf{k} -NS symmetries impose the following nonsymmorphic requirements on the Berry curvature F (see Sec. S6 of [38]):

$$M_x: F(-k_x, \pi + k_y) = -F(k_x, k_y), \quad (6a)$$

$$M_y: F(\pi + k_x, -k_y) = -F(k_x, k_y), \quad (6b)$$

$$P_\pi: F(\pi - k_x, \pi - k_y) = F(k_x, k_y), \quad (6c)$$

which are confirmed in Fig. 2(e).

The model is an insulator at zero energy unless the bulk gap closing condition

$$\sqrt{\gamma_x^2 + \gamma_y^2} = \sqrt{\lambda_x^2 + \lambda_y^2} \quad (7)$$

is satisfied (see Sec. S4 of [38]). The isotropic feature of Eq. (7) implies that the bulk-energy gap closing condition is nonseparable along the x and y directions.

Dipole and quadrupole moments quantized by \mathbf{k} -NS symmetries.—Based on techniques derived in Refs. [20,21], we find that \mathbf{k} -NS M_x , M_y , and P_π quantize electric polarization in a nonlocal manner (see Sec. S8 of [38] for detailed derivation):

$$\{p_x^j(k_y)\} \stackrel{M_x}{=} \{-p_x^j(k_y + \pi)\} \pmod{\mathbf{1}}, \quad (8a)$$

$$\{p_y^j(k_x)\} \stackrel{M_y}{=} \{-p_y^j(k_x + \pi)\} \pmod{\mathbf{1}}, \quad (8b)$$

$$\{p_x^j(k_y)\} \stackrel{P_\pi}{=} \{-p_x^j(\pi - k_y)\} \pmod{\mathbf{1}}, \quad (8c)$$

$$\{p_y^j(k_x)\} \stackrel{P_\pi}{=} \{-p_y^j(\pi - k_x)\} \pmod{\mathbf{1}}. \quad (8d)$$

Here, $p_x(k_y) = \sum_{j=1}^{N_{\text{occ}}} \nu_x^j(k_y)$ is the sum of Wannier centers of the occupied bands and similar for $p_y(k_x)$. This feature stems from the fact that no wave vector \mathbf{k} is invariant under \mathbf{k} -NS reflections, as indicated by the momentum half-translation on the right hand of Eq. (8a). In addition, \mathbf{k} -NS P_π enforces a vanished bulk polarization, as the Berry phases of the two filled bands come in pairs around zero, in accordance with the calculation via Eq. (4) (also see Sec. S3 of [38]).

M_x and M_y further quantize the quadrupole moment nonlocally by restricting the Wannier-sector polarization p_x^y and p_y^x as (Sec. S8 of [38])

$$\{p_x^y(k_y)\} \stackrel{M_x}{=} \{-p_x^y(k_y + \pi)\} \pmod{\mathbf{1}}, \quad (9a)$$

$$\{p_y^x(k_x)\} \stackrel{M_y}{=} \{-p_y^x(k_x + \pi)\} \pmod{\mathbf{1}}. \quad (9b)$$

Whereas $p_x^{\nu_y}$ and $p_y^{\nu_x}$ can be either 0 or 1/2, they must additionally satisfy $p_x^{\nu_y} = p_y^{\nu_x}$ because the phase transition occurs under an isotropic bulk band closure [see Eq. (7) and Fig. 2(e)]. Such isotropic bulk gap closure accompanies the quadrupole phase transition, which distinguishes the current model from the originally reported double-mirror quadrupole insulator model [20,21,30], where the phase transition accompanies a Wannier band closing (when in the absence of C_4 rotational symmetry) and the Wannier-sector polarizations are independent along different directions [21] (see Sec. S7 of [38] for a detailed comparison). Shown in Fig. 2(f) are the gapped Wannier bands symmetric around $\nu_x = 0.5$ in the RP^2 reduced BZ, confirming vanished bulk polarization $p_x = 0$. Such vanished bulk polarization is enforced by $\mathbf{k} - \text{NS}$ symmetry P_π , accordant with the fact that besides being symmetric around $k_i = 0 (i = x, y)$, the Wannier band is also symmetric around $k_i = \pm\pi/2 (i = x, y)$ (see Sec. S9 of [38]). Figure 2(g) shows the Wannier-sector polarizations $p_x^{\nu_y} = 0.5$ for the filled Wannier bands [red in Fig. 2(f)] and confirms the relation in Eq. (9a). Together with similar analyses along the y direction, they give rise to a bulk quadrupole phase diagram shown in Fig. 2(h), where a nontrivial bulk quadrupole moment appears inside the isotropic phase boundary (red circle) accompanied by a bulk gap closure [Eq. (7)]. Therefore, the model realizes an SPTP whose quadrupole moment is protected by the $\mathbf{k} - \text{NS}$ symmetries, and its phase transition accompanies a bulk-energy closure (rather than Wannier-band gap closure), indicating a feature of intrinsic HOTI.

Coexistence of intrinsic and extrinsic HOTI features.—The nonsymmorphic nature of the $\mathbf{k} - \text{NS}$ symmetries can cause boundary obstruction within an SPTP under sample truncation, rendering the simultaneous presence of intrinsic and extrinsic HOTI features. Figure 3(a) shows the phase diagram of edge polarization, which differs from the bulk quadrupole diagram [Fig. 2(h)]. Within the nontrivial region [Fig. 3(b)], a pair of edge modes (green curves) appears, and they map to each other under the $\mathbf{k} - \text{NS}$ reflection M_y that remains preserved in a y -open cylinder. The momentum-resolved probability density of edge bands is located at opposite ends of the cylinder and displays momentum half-translation [Figs. 3(c) and 3(d)], which facilitates the experimental demonstration of $\mathbf{k} - \text{NS}$ symmetry, as we will elaborate below.

Moreover, the phase transition of edge polarization can occur via either bulk or edge gap closures: hopping strength variation along the *periodic* direction leads to an *edge* gap closure [Figs. 3(e)–3(g) that cross a dashed line in Fig. 3(a)], while that along the *open* direction results in a *bulk* gap closure [see Figs. 3(h)–3(j) that cross a solid arc in Fig. 3(a)]. Such coexistence of BOTP and SPTP transitions appears because the $\mathbf{k} - \text{NS}$ reflection along the open direction of a cylinder is preserved and gives rise to an SPTP transition, while that along its periodic direction is broken and a BOTP transition occurs.

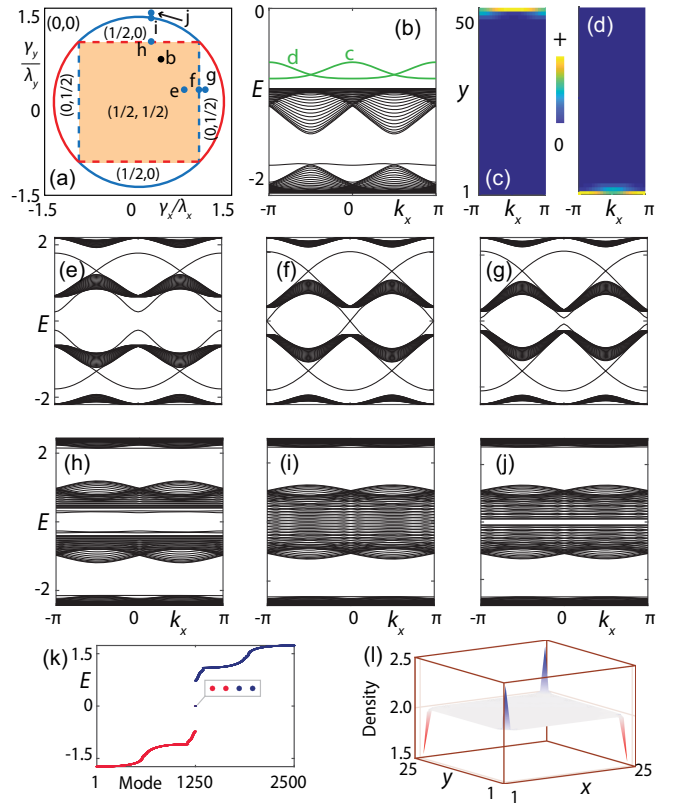


FIG. 3. Edge-polarization phase diagram with coexistence of bulk and edge gap closure. (a) Phase diagram of edge polarization (p_x^e, p_y^e) of the RP^2 quadrupole model. Red and blue refer to x -open and y -open cylinders, respectively. Solid and dashed lines refer to bulk and edge gap closure, respectively. (b)–(d) Edge spectrum (b) of a y -open cylinder under $\gamma_x = 0.25, \gamma_y = 0.5$, where the edge bands (green) are glide-reflection partners (c), (d) located on the opposite ends of the cylinder. (e)–(g) Edge gap closure and reopening under hopping variation along the periodic direction x . (h)–(j) Bulk gap closure and reopening under hopping variation along the open direction y . (k), (l) Appearance of four zero corner modes and their $\pm 1/2$ -quantized charge density under full open boundaries, where $\gamma_x = 0.25, \gamma_y = 0.2$, x -direction unit-cell number $N_x = 25$. $N_y = 25$ is consistently used for panels (b)–(i).

Accordingly, despite the nontrivial bulk quadrupole moment within the isotropic circle of the bulk phase diagram [Fig. 2(h)], four degenerate corner modes [Figs. 3(k), (l)] only appear within the shaded square of the edge phase diagram [Fig. 3(a)] under full open boundaries.

Experimental proposals.—We propose an experimental design to realize the RP^2 BZ and the associated high-order topology based on acoustic resonator arrays [25–27,53,54]. The cavity resonator emulating the site of Fig. 2(c) is designed to work at the dipole mode where nearest-neighbor positive and negative couplings are possible [Fig. 4(a)] [27,53] (see Sec. S11.A of [38] for details). The coupling strength can be tuned by the tube cross section and its position with respect to the middle of the

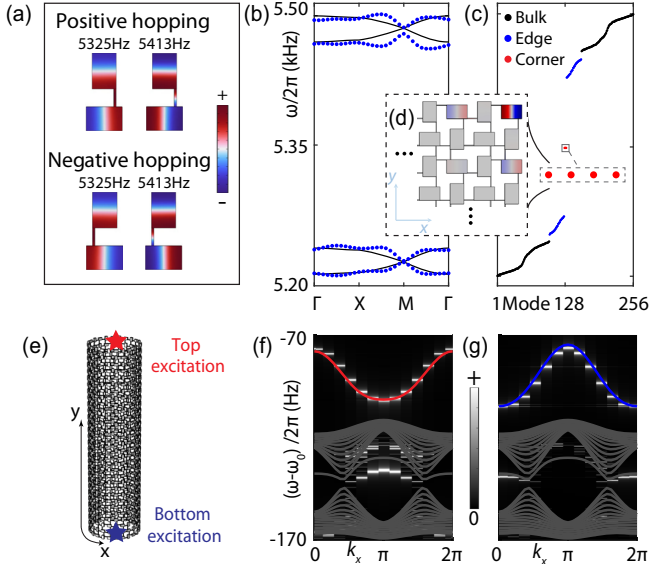


FIG. 4. Acoustic experimental proposal for realizing the RP^2 quadrupole insulator and measuring signatures of the $\mathbf{k} - \text{NS}$ symmetries. (a) Acoustic design for positive (negative) hoppings through right-located (left-located) connecting tube between two perpendicularly arranged identical resonators. (b) Bulk bands (blue dots) of an acoustic crystal (made of building blocks in (a) in agreement with tight-binding predictions (black curves). (c),(d) Full-open spectra (c) of a 7×7 array contain in-gap corner modes with sound pressure localization at the corner (d). (e) Cylinder structure for demonstrating the momentum half-translation of $\mathbf{k} - \text{NS}$ M_y symmetry. Red and blue stars indicate point source excitations on the opposite ends of the cylinder. (f), (g) Fourier-transformed pressure distributions show the excitation of edge bands [red curve under top excitation in (f) and blue curve under bottom excitation in (g)] and their momentum half-translation. Other acoustic bands are in gray.

resonator. To get a wide band gap, a large coupling contrast is designed between intracell and intercell hoppings, which are ≈ 10 Hz and 86 Hz, respectively. Based on these link building blocks, we design the model [Fig. 2(c)] by constructing an acoustic resonator array featuring the checkerboard π flux configuration. Its bulk bands are shown by blue dots in Fig. 4(b), in good agreement with the tight-binding theory (solid curves) under an on-site potential of $\omega_0/2\pi \approx 5.37$ kHz. The open-boundary spectra for a 7×7 array is plotted in Fig. 4(c), where four in-gap corner modes appear, as verified by the corner-localized sound pressure distribution [Fig. 4(d)].

Moreover, the momentum half-translation of the $\mathbf{k} - \text{NS}$ symmetries can be experimentally measured. Consider a cylinder structure [Fig. 4(e)] that can be manufactured via 3D printing. We simulate the structure response under a point-source excitation on either the top (red) or bottom (blue) end of the cylinder [Fig. 4(e)]. The Fourier transform of the recorded pressure distribution of the cylinder (see Sec. S11.C of [38]) generates the momentum-resolved edge spectra [Figs. 4(f) and 4(g)]. Inside the bulk gap, an edge

band [red in Fig. 4(f) or blue in Fig. 4(g)] appears under excitation on the opposite ends of the cylinder, respectively, and they exhibit a π shift in momentum, which faithfully realize the tight-binding predictions in Figs. 3(b)–3(d) and thus demonstrate the presence of the $\mathbf{k} - \text{NS}$ M_y reflection. Besides the nonsymmorphic constraints on the Berry curvature [Eq. (6) and Fig. 2(e)], the BOTP edge closure [Figs. 3(e)–3(g)], and the SPTP bulk closure [Figs. 3(h)–3(j)] can also be experimentally probed by measuring a real-space torus and cylinder, which we discuss in Sec. S11.D and Sec. S11.B of [38], respectively. The realization of the $\mathbf{k} - \text{NS}$ quadrupole insulator is not limited to the acoustic design presented here; the same physics can be demonstrated with coupled optical ring resonators, mechanical metamaterials, and circuits, and we provide more detailed discussions on these platforms in Sec. S11.E of [38].

Conclusions.—We report a HOTI on a Brillouin RP^2 protected by $\mathbf{k} - \text{NS}$ symmetries via \mathbf{Z}_2 synthetic gauge fields. A natural generalization of the present work is to construct HOTIs on various BZ manifolds like RP^n in three-dimensional momentum space and synthetic dimensions. Another area of exploration would be to utilize $\mathbf{k} - \text{NS}$ symmetries to stabilize semimetallic degeneracies [55], such as nodal lines and nodal loops. The gauge fields used here are \mathbf{Z}_2 $U(1)$ fields, and it is thus interesting to construct $\mathbf{k} - \text{NS}$ symmetries with matrix-valued non-Abelian gauge fields. Furthermore, delving into the non-Hermitian regime (see a brief discussion in Sec. S10 of [38]), it becomes relevant to explore how exceptional points and the complex energy winding and braiding can be influenced by the $\mathbf{k} - \text{NS}$ symmetries and the resulting BZ manifolds.

Note added.—During the completion and peer review of this letter, we noticed several works studying higher-order topology in models featuring momentum-space nonsymmorphic symmetries [56–59].

The authors thank Hengbin Cheng, Yixin Sha, Ce Shang, Xiaoming Wang, Zheng Zhang, and Yuxin Zhao for fruitful discussions. The authors acknowledge the support from the National Natural Science Foundation of China Excellent Young Scientists Fund (HKU 12222417), the Hong Kong Research Grant Council Strategic Topics Grant No. STG3/E-704/23-N, the startup fund of The University of Hong Kong, and the Asian Young Scientist Fellowship. J. H. acknowledges the support from the National Natural Science Foundation of China (Grant No. 61805141).

* yiyg@hku.hk

- [1] L. Fu, *Phys. Rev. Lett.* **106**, 106802 (2011).
- [2] T. H. Hsieh, H. Lin, J. Liu, W. Duan, A. Bansil, and L. Fu, *Nat. Commun.* **3**, 982 (2012).
- [3] Y. Tanaka, Z. Ren, T. Sato, K. Nakayama, S. Souma, T. Takahashi, K. Segawa, and Y. Ando, *Nat. Phys.* **8**, 800 (2012).

- [4] P. Dziawa, B. Kowalski, K. Dybko, R. Buczko, A. Szczerbakow, M. Szot, E. Łusakowska, T. Balasubramanian, B. M. Wojek, M. Berntsen *et al.*, *Nat. Mater.* **11**, 1023 (2012).
- [5] C. Fang and L. Fu, *Phys. Rev. B* **91**, 161105(R) (2015).
- [6] C.-X. Liu, R.-X. Zhang, and B. K. VanLeeuwen, *Phys. Rev. B* **90**, 085304 (2014).
- [7] K. Shiozaki, M. Sato, and K. Gomi, *Phys. Rev. B* **91**, 155120 (2015).
- [8] S. A. Parameswaran, A. M. Turner, D. P. Arovas, and A. Vishwanath, *Nat. Phys.* **9**, 299 (2013).
- [9] D. Varjas, F. de Juan, and Y.-M. Lu, *Phys. Rev. B* **92**, 195116 (2015).
- [10] K. Shiozaki, M. Sato, and K. Gomi, *Phys. Rev. B* **93**, 195413 (2016).
- [11] A. Kitaev, *AIP Conf. Proc.* **1**, 22 (2009).
- [12] A. P. Schnyder, S. Ryu, A. Furusaki, and A. W. W. Ludwig, *Phys. Rev. B* **78**, 195125 (2008).
- [13] Z. Chen, S. A. Yang, and Y. Zhao, *Nat. Commun.* **13**, 2215 (2022).
- [14] M. Aidelsburger, S. Nascimbene, and N. Goldman, *C.R. Phys.* **19**, 394 (2018).
- [15] Y. X. Zhao, Y.-X. Huang, and S. A. Yang, *Phys. Rev. B* **102**, 161117(R) (2020).
- [16] Z. Chen, Z. Zhang, S. A. Yang, and Y. Zhao, *Nat. Commun.* **14**, 743 (2023).
- [17] R. Resta, *Ferroelectrics* **136**, 51 (1992).
- [18] R. D. King-Smith and D. Vanderbilt, *Phys. Rev. B* **47**, 1651 (1993).
- [19] D. Vanderbilt, *Berry Phases in Electronic Structure Theory: Electric Polarization, Orbital Magnetization and Topological Insulators* (Cambridge University Press, Cambridge, England, 2018).
- [20] W. A. Benalcazar, B. A. Bernevig, and T. L. Hughes, *Science* **357**, 61 (2017).
- [21] W. A. Benalcazar, B. A. Bernevig, and T. L. Hughes, *Phys. Rev. B* **96**, 245115 (2017).
- [22] F. Schindler, A. M. Cook, M. G. Vergniory, Z. Wang, S. S. Parkin, B. A. Bernevig, and T. Neupert, *Sci. Adv.* **4**, eaat0346 (2018).
- [23] C. W. Peterson, W. A. Benalcazar, T. L. Hughes, and G. Bahl, *Nature (London)* **555**, 346 (2018).
- [24] S. Mittal, V. V. Orre, G. Zhu, M. A. Gorlach, A. Poddubny, and M. Hafezi, *Nat. Photonics* **13**, 692 (2019).
- [25] Y. Qi, C. Qiu, M. Xiao, H. He, M. Ke, and Z. Liu, *Phys. Rev. Lett.* **124**, 206601 (2020).
- [26] X. Ni, M. Li, M. Weiner, A. Alù, and A. B. Khanikaev, *Nat. Commun.* **11**, 2108 (2020).
- [27] H. Xue, Y. Ge, H.-X. Sun, Q. Wang, D. Jia, Y.-J. Guan, S.-Q. Yuan, Y. Chong, and B. Zhang, *Nat. Commun.* **11**, 2442 (2020).
- [28] M. Serra-Garcia, V. Peri, R. Süsstrunk, O. R. Bilal, T. Larsen, L. G. Villanueva, and S. D. Huber, *Nature (London)* **555**, 342 (2018).
- [29] S. Imhof, C. Berger, F. Bayer, J. Brehm, L. W. Molenkamp, T. Kiessling, F. Schindler, C. H. Lee, M. Greiter, T. Neupert *et al.*, *Nat. Phys.* **14**, 925 (2018).
- [30] E. Khalaf, W. A. Benalcazar, T. L. Hughes, and R. Queiroz, *Phys. Rev. Res.* **3**, 013239 (2021).
- [31] M. Geier, L. Trifunovic, M. Hoskam, and P. W. Brouwer, *Phys. Rev. B* **97**, 205135 (2018).
- [32] R. Queiroz, I. C. Fulga, N. Avraham, H. Beidenkopf, and J. Cano, *Phys. Rev. Lett.* **123**, 266802 (2019).
- [33] Z.-K. Lin, H.-X. Wang, Z. Xiong, M.-H. Lu, and J.-H. Jiang, *Phys. Rev. B* **102**, 035105 (2020).
- [34] X. Zhang, Z.-K. Lin, H.-X. Wang, Z. Xiong, Y. Tian, M.-H. Lu, Y.-F. Chen, and J.-H. Jiang, *Nat. Commun.* **11**, 65 (2020).
- [35] Y. Liu, B. Lei, P. Yu, L. Zhong, K. Yu, and Y. Wu, *Mech. Syst. Sig. Proc.* **198**, 110433 (2023).
- [36] N. Mao, H. Wang, Y. Dai, B. Huang, and C. Niu, *npj Comput. Mater.* **8**, 154 (2022).
- [37] Z. Liu, G. Wei, and J.-J. Xiao, *Phys. Rev. B* **106**, 085415 (2022).
- [38] See Supplemental Materials at <http://link.aps.org/supplemental/10.1103/PhysRevLett.132.213801> for notes on (1) RP^2 Brillouin zone (BZ) by momentum-space nonsymmorphic symmetries, (2) BZ partition, (3) symmetry eigenvalue of nonsymmorphic inversion, (4) analytical bulk spectra, (5) gauge transformation, (6) nonsymmorphic Berry curvature, (7) comparison between the RP^2 and double-mirror quadrupole insulator models, (8)–(10) calculation of bulk, edge, and Wannier-sector polarization on RP^2 and torus BZ, (11) non-Hermitian extension, and (12) experimental proposals on engineered platforms, which includes Refs. [39–46].
- [39] W. A. Benalcazar, T. Li, and T. L. Hughes, *Phys. Rev. B* **99**, 245151 (2019).
- [40] Y. Yang, B. Yang, G. Ma, J. Li, S. Zhang, and C. Chan, *Science* **383**, ead9621 (2024).
- [41] Y. Yang, C. Peng, D. Zhu, H. Buljan, J. D. Joannopoulos, B. Zhen, and M. Soljačić, *Science* **365**, 1021 (2019).
- [42] Z. Pang, B. T. T. Wong, J. Hu, and Y. Yang, *Phys. Rev. Lett.* **132**, 043804 (2024).
- [43] J. Du, T. Li, X. Fan, Q. Zhang, and C. Qiu, *Phys. Rev. Lett.* **128**, 224301 (2022).
- [44] J.-H. Chen, Z.-Z. Yang, W.-J. Yang, A.-Y. Guan, X.-Y. Zou, and J.-C. Cheng, *Appl. Phys. Lett.* **120**, 253508 (2022).
- [45] T. Li, L. Liu, Q. Zhang, and C. Qiu, *Commun. Phys.* **6**, 268 (2023).
- [46] M. Hafezi, S. Mittal, J. Fan, A. Migdall, and J. Taylor, *Nat. Photonics* **7**, 1001 (2013).
- [47] B. J. Wieder, B. Bradlyn, Z. Wang, J. Cano, Y. Kim, H.-S. D. Kim, A. M. Rappe, C. Kane, and B. A. Bernevig, *Science* **361**, 246 (2018).
- [48] L. Lu, C. Fang, L. Fu, S. G. Johnson, J. D. Joannopoulos, and M. Soljačić, *Nat. Phys.* **12**, 337 (2016).
- [49] Z. Wang, A. Alexandradinata, R. J. Cava, and B. A. Bernevig, *Nature (London)* **532**, 189 (2016).
- [50] Y. Yang, B. Zhen, J. D. Joannopoulos, and M. Soljačić, *Light Sci. Appl.* **9**, 177 (2020).
- [51] Y. Yang, H. C. Po, V. Liu, J. D. Joannopoulos, L. Fu, and M. Soljačić, *Phys. Rev. B* **106**, L161108 (2022).
- [52] L. Fu and C. L. Kane, *Phys. Rev. B* **76**, 045302 (2007).
- [53] H. Xue, Z. Wang, Y.-X. Huang, Z. Cheng, L. Yu, Y. X. Foo, Y. X. Zhao, S. A. Yang, and B. Zhang, *Phys. Rev. Lett.* **128**, 116802 (2022).
- [54] T. Li, J. Du, Q. Zhang, Y. Li, X. Fan, F. Zhang, and C. Qiu, *Phys. Rev. Lett.* **128**, 116803 (2022).

- [55] André Grossi e Fonseca, Sachin Vaidya, Thomas Christensen, Mikael C. Rechtsman, Taylor L. Hughes, and Marin Soljačić, [arXiv:2310.18485](#).
- [56] Y. Wang, C. Zhang, Z. Y. Chen, B. Liang, Y. X. Zhao, and J. Cheng, [arXiv:2305.07174](#).
- [57] Z. Zhu, L. Yang, J. Wu, Y. Meng, X. Xi, B. Yan, J. Chen, J. Lu, X. Huang, W. Deng, C. Shang, P. P. Shum, Y. Yang, H. Chen, G.-G. Liu, Z. Liu, and Z. Gao, [arXiv:2305.08450](#).
- [58] Y.-L. Tao, M. Yan, M. Peng, Q. Wei, Z. Cui, S. A. Yang, G. Chen, and Y. Xu, *Phys. Rev. B* **109**, 134107 (2024).
- [59] Y.-L. Tao, J.-H. Wang, and Y. Xu, [arXiv:2307.00486](#).